



## Absolute instability of impinging leading edge vortices in a submodel of a bileaflet mechanical heart valve

Hadi Zolfaghari <sup>\*</sup> and Dominik Obrist 

*ARTORG Center for Biomedical Engineering Research, 3010 Bern, Switzerland*



(Received 24 July 2019; published 6 December 2019)

Bileaflet mechanical heart valves (BMHVs) have been related to the production of unphysiological turbulent flow in the ascending aorta. These valves comprise a pair of rigid blunt plates (leaflets), which are immersed in a confined flow with Reynolds numbers up to 10 000. They are prone to develop impinging leading-edge vortex (ILEV) instabilities [K. Hourigan *et al.*, *J. Fluids Struct.* **15**, 387 (2001); S. Deniz and T. Staubli, *ibid.* **11**, 3 (1997)] on the leaflets because of their relatively large chord-to-thickness ratio and their low angle of incidence. These instabilities can produce strong disturbances between the leaflets which may contribute to the onset and intensity of turbulent flow in the wake of the valve. The complex nature of the flow around BMHVs prevents a detailed theoretical analysis of the underlying instability mechanisms. Therefore, we defined a two-dimensional submodel of the flow with fixed leaflets, which renders the problem accessible to the rich toolbox of hydrodynamic stability theory. High-order numerical simulations of this flow configuration indicated the systolic development of unstable ILEVs on the inner side of the leaflets during systolic acceleration of the flow. We found that the ILEV instabilities can only be observed with sufficiently high spatial resolution, which may explain why these phenomena have not been observed so far in most computational studies of BMHV flow. Orr-Sommerfeld eigenmodes with high growth rates confirmed the unstable character of this flow. We further identified a pocket of absolute instability which acts as a wave maker between the leaflets. Finally, we confirmed that this wave-maker region has a direct effect on the nonlinear breakdown in the wake of the valve. To this end, the leaflet geometry was modified such that the ILEV (and the associated wave maker) was eliminated and it was shown numerically that the wake remains laminar for the modified geometry. The results of this study are a first step toward a detailed understanding of the hydrodynamic instability mechanisms which lead to turbulent flow past BMHVs.

DOI: [10.1103/PhysRevFluids.4.123901](https://doi.org/10.1103/PhysRevFluids.4.123901)

### I. INTRODUCTION

#### A. Background

Native heart valves, such as the aortic or mitral valve, may fail due to stenosis or insufficiency. In severe cases, the diseased valve has to be replaced by a mechanical or biological prosthetic valve [1]. Mechanical valves feature rigid leaflets, unlike biological valves which possess soft tissue cusps. Mechanical heart valves are superior to biological valves with respect to durability. However, they create adverse flow conditions possibly leading to blood damage and thrombosis. Therefore, recipients of mechanical heart valves receive lifelong anticoagulation therapy to reduce the risks of thromboembolism and stroke [1,2]. Blood damage and thrombogenicity in a mechanical valve are

---

<sup>\*</sup>hadi.zolfaghari@artorg.unibe.ch

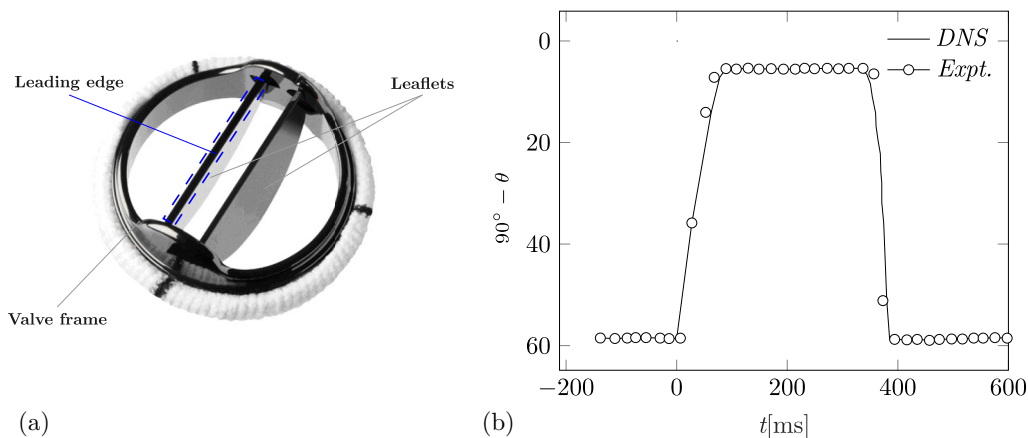


FIG. 1. (a) Leading-edge view of a St. Jude Medical Regent mechanical valve [17]. The valve leaflets are hinged in a metal frame housing, which is sutured to the aortic root. (b) Leaflet kinematics of BMHV: (—) numerical FSI simulation of Borazjani *et al.* [7] and (○) experimental investigation of Dasi *et al.* [3].

believed to be correlated to critically elevated shear-stress levels in the blood flow, which is often described as turbulent. Mitigation of the turbulent flow in the mechanical valve may reduce the need for anticoagulation therapy.

### B. State of the art

The fluid dynamics of bileaflet mechanical heart valves [BMHVs, Fig. 1(a)] has been largely investigated by means of experiments [3–5] and numerical simulations [6–9]. All studies emphasize the presence of unsteady flow events past the mechanical valve, where various hydrodynamic instability waves emerge, evolve, and interact in a confined manner. One can observe, for example, shear layer instabilities in the wake of the leaflets [3], flow oscillations in and over the sinuses of Valsalva (cavities in the aortic wall downstream of the valve), as well as instabilities due to flow pulsatility. More recent work highlighted the importance of small-scale structures on the hemodynamic performance of BMHVs [5,9]. Bellofiore *et al.* [5] performed a series of high-resolution particle image velocimetry (PIV) experiments in an up-scaled model of a fully open BMHV model. Their instantaneous velocity fields showed large vortices coming from the region between the two leaflets (central orifice) which enter the wake of the valve. They suspected that the boundary-layer separation due to adverse pressure gradients between the leaflets might be the primary mechanism for the generation of these vortices. It can be hypothesized that such vortices may also be a result of the flow impingement at the blunt leading edge of the leaflets, similar to the instabilities observed in the flow around blunt plates at moderate Reynolds numbers [10–12]. These instabilities, for blunt plates of high aspect ratio and at low angle of incidence, are known as impinging leading-edge vortex (ILEV) instabilities [13,14]. ILEV instabilities are believed to involve Kelvin-Helmholtz instabilities in the separated shear layers, and instabilities which are responsible for large-scale shedding [13,15].

### C. Bottom-up approach to study BMHV flow instabilities

A detailed understanding of the instability mechanisms in BMHVs is a prerequisite for understanding the laminar-turbulent transition in this valve. Nevertheless, the hydrodynamic stability of BMHVs has received only limited attention, mainly due to the complex nature of the flow system comprising fluid-structure interaction, laminar-turbulent transition, and turbulence. Most previous investigations have tried to include as much complexity in their models as possible to reproduce all

phenomena. Although this has resulted in a great body of quantitative and qualitative knowledge, it has left several basic and important questions unanswered because multiple phenomena are at work simultaneously, which makes it nearly impossible to isolate different mechanisms. As a result, it remains unclear what types of flow instabilities are present and what role they play in the laminar-turbulent transition process. Therefore, it remains also unknown where these instabilities originate and how they could be suppressed. We propose to approach these questions in a bottom-up approach which breaks down the full problem into submodels such that the phenomena can be studied in an isolated and focused manner. In the same manner as results of hydrodynamic stability theory for canonical boundary layers are successfully applied in the design of full airplane wings, we hope that the present study of a BMHV submodel can be a first step toward establishing a solid theoretical basis which can eventually contribute to a better understanding of the flow past heart valves in its full complexity.

To this end, we define a two-dimensional submodel of a BMHV to resolve ILEV structures and study their linear stability on the leaflets of BMHVs during the acceleration phase of systole. This time window is believed to accommodate the early stages of laminar-turbulent transition in the wake [8].

The limited complexity of this submodel allows one to use well-established tools of hydrodynamic stability theory, which can provide deeper insight into the basic mechanisms of the underlying flow configuration. Moreover, the reduced complexity allows us to use very high numerical resolution (see Sec. II), such that flow features can be resolved which have slipped previously through the coarser meshes of complex top-down models of heart valves.

#### D. Outline

In this study, we performed two-dimensional direct numerical simulations (2D-DNS) of the flow in this submodel of the BMHV. The simulation results showed vortex shedding on the inner side (closer to centerline) of both leaflets. The shed vortical structures were observed to grow in size while traveling downstream, and to drive the breakdown of Burgers-like vortices issuing from the trailing edge of the leaflets. This breakdown resulted in a chaotic wake flow, rich in small- and large-scale vortices. To better understand these processes, we studied the stability of ILEV structures that were identified in the 2D-DNS using viscous parallel linear stability theory. Unstable temporal eigenmodes were found in the area between the separation point and the first emergence of waviness in the detached shear layer downstream of the leading edge. Remarkable agreement was found between results from linear stability theory and 2D-DNS data with respect to the phase speed of the most unstable eigenmodes. Inspired by the existence of reverse flow zones in the ILEV, the absolute or convective nature of these instabilities was examined with the method of cusp maps [16], which was applied to time-averaged separated flow profiles. This analysis revealed a pocket of absolute instability located approximately three thickness lengths downstream of the leading edge of the leaflets. To demonstrate the pivotal role of absolute instabilities in laminar-turbulent transition in BMHVs, we proposed a modified leaflet geometry which eliminates the wave-maker region between the leaflets of the BMHV. 2D-DNS of the systolic flow in this configuration showed no sign of recirculation or flow oscillations between the leaflets. In the absence of ILEV instabilities, the wake structures also remained laminar. The linear stability analysis of the boundary-layer profiles in the modified model confirmed a linearly stable flow at the leading edge. Convective instabilities with significantly lower growth rates than those in the original model were found only farther downstream. This outcome supports the hypothesis that the elimination of absolute instabilities in the ILEV results in less vorticity production behind a BMHV.

The remainder of this paper is organized as follows. In Sec. II, we define the governing equations, the geometrical model, and the boundary conditions used for direct numerical simulations. In Sec. III, we discuss the presence of ILEV structures on the inner surface of the leaflets, as well as their interaction with other instability mechanisms. In Sec. IV, we investigate the temporal linear stability of the flow profiles along the ILEV and compare them to 2D-DNS data. In Sec. V, we apply

the method of cusp maps to investigate the absolute or convective instability of the time-averaged flow profiles, where we identified pockets of absolute instability. We then propose an alternative leading-edge geometry, which successfully eliminates the flow separation and absolute instability between the leaflets, and also eliminates the breakdown of laminar structures behind the valve. Section VI concludes this paper.

## II. PROBLEM DEFINITION

### A. Governing equations and flow solver

We model the flow with the nondimensional Navier-Stokes equations for incompressible flows,

$$\frac{\partial \tilde{\mathbf{u}}}{\partial \tilde{t}} + \tilde{\mathbf{u}} \cdot \tilde{\nabla} \tilde{\mathbf{u}} = -\tilde{\nabla} \tilde{p} + \frac{1}{Re} \tilde{\nabla}^2 \tilde{\mathbf{u}} + \tilde{\mathbf{f}}, \quad \tilde{\nabla} \cdot \tilde{\mathbf{u}} = 0, \quad (1)$$

where  $\tilde{\mathbf{u}}$  denotes the velocity field,  $\tilde{p}$  stands for pressure, and  $\tilde{\mathbf{f}}$  is the body force density. Note that nondimensional quantities and operators are indicated by  $\tilde{\cdot}$ . The Reynolds number is defined as

$$Re = \frac{\mathcal{U}_0 \mathcal{L}_0}{\nu}, \quad (2)$$

where  $\mathcal{U}_0 = 0.75$  m/s,  $\mathcal{L}_0 = 3 \times r_r = 36$  mm, and  $\nu = 2.7 \times 10^{-6}$  m<sup>2</sup>/s are the velocity scale, length scale, and the kinematic viscosity ( $\nu = \rho/\mu$ ), respectively. The velocity scale  $\mathcal{U}_0$  corresponds to one-half of the inflow velocity at peak flow rate.

Equations (1) are solved using a sixth-order finite-difference scheme in space on a staggered Cartesian grid, and a third-order explicit low-storage Runge-Kutta scheme in time [18]. The solver has been exhaustively validated and used to study various transitional flows [19–23]. Sharp-interface immersed-boundary techniques are used [24–26] for the integration of complex surfaces (e.g., valve leaflets) into the Cartesian grid solver. The order of grid convergence close to the boundaries is limited to second order due to the immersed-boundary method.

### B. Two-dimensional BMHV submodel

#### 1. Planar geometry

The problem geometry (Fig. 2) corresponds to a perpendicular cut through the valve and the aortic root open in their plane of symmetry. This geometry is justified by the flat design of the leaflets, the inherent symmetry of the BMHV, as well as the two-dimensional structure of ILEV instabilities which were observed in the proximity of blunt plates [13]. Furthermore, this plane features the highest local Reynolds numbers because of the high velocities near the centerline, and is therefore a good candidate for studying ILEV instabilities.

#### 2. Kinematic assumptions

Leaflet kinematics of the BMHV [Fig. 1(b)] include a rapid opening ( $\Delta t \approx 20$  ms) at the onset of systole [27], a longer phase ( $\Delta t \approx 350$  ms for a typical heart rate at rest) where the leaflets remain fully open, and an abrupt closing ( $\Delta t \approx 25$  ms) [3,7,28]. The valve leaflets remain in the fully open position at a low angle of incidence ( $5^\circ$ ) during a large part of systole, which is the suitable configuration for creating ILEV instabilities, as for larger angles of incidence the flow phenomena will be different than ILEV [29]. From the time period that the leaflets are fully open, we narrow our focus to the systolic acceleration phase, which spans approximately 200 ms.

The angle of incidence for the fully open BMHV is fixed at  $90^\circ - \theta = 5^\circ$ , which corresponds to the opening angle of a widely used type of BMHV. Experimental studies have confirmed that this angle remains fixed and stable throughout systole [3,27]. Modifications of the BMHV design to reduce this angle are known to interfere with the valve kinematics [30].

The ILEV development at the leading edge is observed to be a rapid process; therefore, its instabilities are expected to be active nearly as long as the valve is fully open. The early dynamics

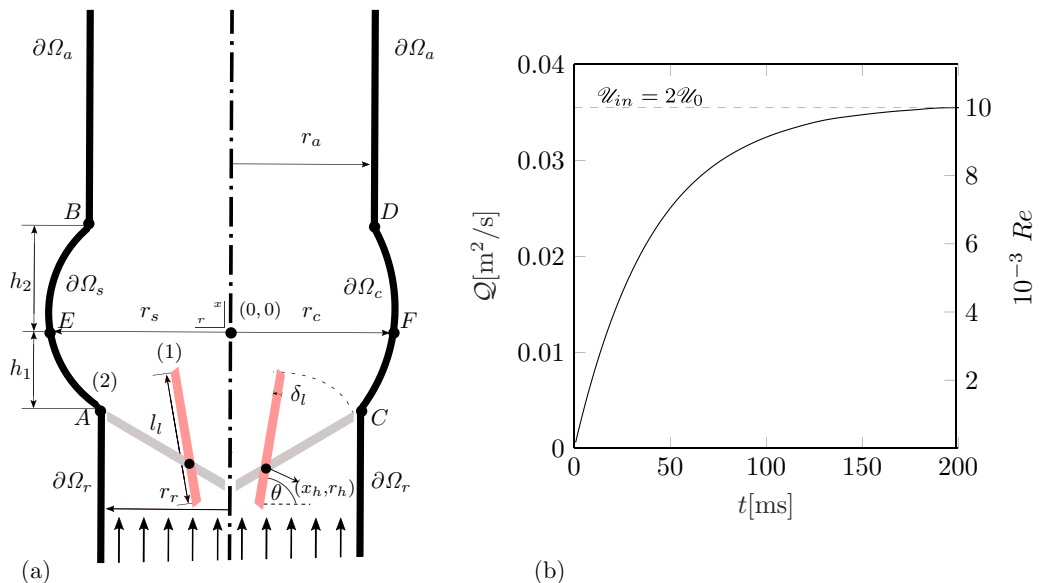


FIG. 2. (a) Submodel of the BMHV in the aortic root. The 2D cross sections of leaflets in their plane of symmetry are shown in (1) open and (2) closed states. Cavities AEB (deeper) and CFD (shallower) represent aortic sinus and valve commissure, respectively. All geometrical parameters of the model are given in Table I. (b) Acceleration wave form used in the 2D-DNS. The horizontal dashed line marks the peak flow rate, corresponding to a mean flow velocity  $\mathcal{U}_{in} = 2\mathcal{U}_0$ .

of these instabilities might be affected by the valve opening process, which involves a few transient vortices which are created during opening and then convected away quickly past the valve [31]. Given the short presence of these structures near the leading edge, we proceed to neglect these effects in our study. Therefore, we assume leaflets in the fully open position in our model, similar to the model with fixed leaflets used by [5].

### 3. Aortic root model

We define our two-dimensional model based on the aortic root model proposed by Haj-Ali *et al.* [32]. In the aortic root model, we placed the leaflets of a St. Jude Medical Regent valve [Fig. 1(a)] in the fully open position [red in Fig. 2(a)]. The bigger cavity on the left side ( $\partial\Omega_s$ ) represents the

TABLE I. Geometrical parameters of the two-dimensional model.

Parameter	Notation	Value
Root radius	$r_r$	12 mm
Sinus radius	$r_s$	$1.40r_r$
Commissure radius	$r_c$	$1.25r_r$
Ascending aorta radius	$r_a$	$1.10r_r$
Cavity downstream length	$h_1$	$0.60r_r$
Cavity upstream length	$h_2$	$0.80r_r$
Leaflet length	$l_l$	$1.15r_r$
Leaflet thickness	$\delta_l$	$0.09r_r$
Hinge longitudinal position	$x_h$	$-1.57r_r$
Hinge radial position	$r_h$	$-0.11r_r$

sinus of Valsalva, while the shallower cavity on the right represents a valve commissure ( $\partial\Omega_c$ ). The base of the aortic root ( $\partial\Omega_r$ ) is modeled by two parallel walls upstream of the cavities. Downstream of the cavities, two parallel walls model the ascending aorta, which has a larger diameter than the aortic root [32]. Throughout this paper, we refer to the sides of the leaflets facing the centerline as the inner side, and to those facing the cavities as the outer side. Since our model is designed to capture instabilities close to the leaflets, which are relatively far from the aortic wall, we neglect aortic wall distensibility and assume that the root geometry is rigid.

#### 4. Boundary conditions and flow forcing

The flow is smoothly accelerated from zero to the mean velocity of  $\mathcal{U}_{in} = 2\mathcal{U}_0$  at  $t = 200$  ms [Fig. 2(b)]. No-slip boundary conditions are imposed on the rigid valve leaflets and aortic root boundaries. Periodic boundary conditions are used in the flow direction, and the systolic wave form is forced using a fringe region technique [33] upstream of the valve,

$$\tilde{\mathbf{f}} = \lambda(x)(\tilde{\mathbf{u}} - \hat{\mathbf{u}}(t)), \quad (3)$$

where  $\lambda(x)$  is the fringe function and  $\hat{\mathbf{u}}(t)$  is a uniform flow profile. The amplitude of  $\hat{\mathbf{u}}(t)$  and the fringe function  $\lambda(x)$  are tuned *ad hoc* to yield the desired systolic acceleration [Fig. 2(b)]. The fringe forcing enforces the given inflow profile, while it simultaneously damps out the outflow disturbances reentering the domain at the inflow, due to periodic boundary conditions.

#### C. Grid resolution

A very high grid resolution with approximately 5.1 M ( $1024 \times 5120$ ) grid points in a rectangular domain of size  $3r_r \times 15r_r$  was used to deal with the nonconforming geometry of the leaflets and also to resolve the spatiotemporal instability waves and their interactions. The grid accommodated 31 grid points along the blunt edge of each leaflet (corresponding to a uniform grid spacing of  $\delta_h \approx 35 \mu\text{m}$ ) to ensure that the flow impingement is fully resolved. A Courant-Friedrichs-Lewy (CFL) number of 0.1 has been set. We chose a low value for the CFL number to reduce time-integration errors. This resulted in an average time-step size of  $dt \approx 5 \times 10^{-6}$  s. The computations required 6000 core  $\times$  hours on a Cray XC40/50 supercomputer to simulate 200 ms of the cardiac cycle.

### III. INSTABILITIES IN THE BMHV SUBMODEL

#### A. Evolution of vorticity fields

Figure 3 shows three snapshots taken from 2D-DNS of the flow throughout the systolic acceleration, illustrating the evolution of vorticity ( $\boldsymbol{\omega} = \nabla \times \mathbf{u}$ ). These snapshots indicate the following phenomena:

- (1) an instability starting at the trailing edge of each leaflet which leads to an array of Burgers-like vortices [34, p. 272];
- (2) vortex sheet roll-up in both cavities without notable interaction with the bulk flow structures, except at late stages;
- (3) stable Falkner-Skan-type boundary layers with favorable pressure gradients on the outer side of the leaflets;
- (4) unstable impinging leading-edge vortices (ILEVs) developing on the inner side of the leaflets, which involves self-sustained oscillations between the leaflets; and
- (5) breakdown in the wake due to nonlinear interaction of the vortices emanated from the ILEVs, with both arrays of Burgers vortices.

Burgers vortices behind the valve sustain their symmetric laminar structure prior to the arrival and interaction of high-speed vortices, which are detached from the inner side of the leaflets. This observation is in line with stability characteristics of Burgers vortices, which has been investigated both asymptotically [35] and at all Reynolds numbers [36]. They were shown to be stable to three-dimensional perturbations, despite the possibility of transient growth. Therefore, it can be

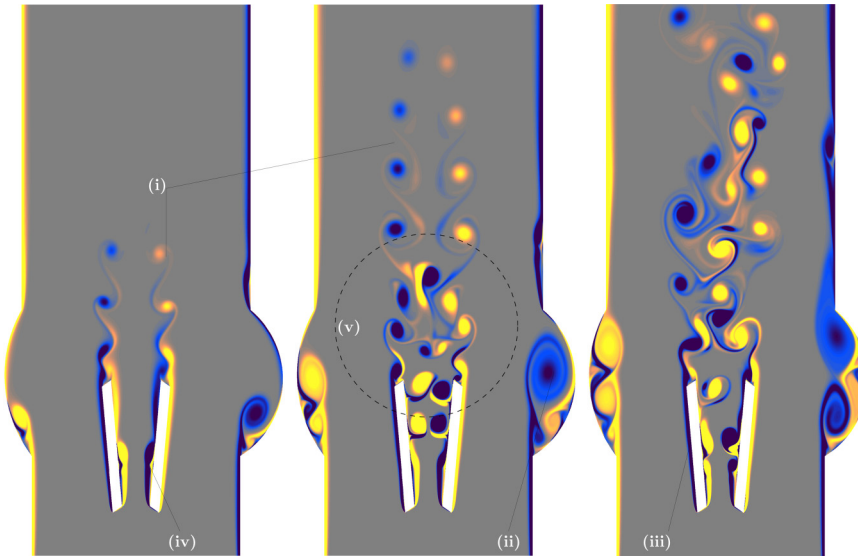


FIG. 3. Snapshots of vorticity (left to right:  $t = 35, 57, 79$  ms). Dark blue and light yellow show the vorticity extrema. Present flow instabilities include (i) Burgers vortices straining in the wake, (ii) vortex sheet roll-up in the cavities, (iii) Falkner-Skan-type boundary layers (FSBLs) with favorable pressure gradient on the outer side of the valve leaflets, (iv) stretched ILEV on the inner side of the leaflets, and (v) nonlinear breakdown in the wake, due to the interaction of vortices shed from the ILEV with Burgers vortices.

speculated that their breakdown can be avoided by the elimination of ILEV instabilities. This speculation is based on the present 2D theoretical model and it is not unlikely that ILEV may evolve to 3D structures downstream of their initial growth zone [13]. Nevertheless, Hourigan *et al.* [13] suggest that the separating shear layer is invariant in the spanwise direction in the vicinity of the leading edge; therefore, we assume that the initial instability is two dimensional. Secondary instability of the ILEV disturbances and exact dynamics of their interaction with the wake structures will be the subject of future work.

A closer inspection of the impinging flow at the leading edge (Fig. 4, right panel) shows that an ILEV features velocity profiles similar to those in a separation bubble on aircraft wings at moderate Reynolds numbers [37–41]. To describe the flow near the leading edge, we introduce local coordinates  $\xi$  and  $\eta$ , which originate on the centerline at the  $x$  coordinate of the inner corner of the leading edge of the leaflet (Fig. 4, left panel). The streamwise coordinate  $\xi$  is aligned with the direction of the bulk flow and the cross-stream coordinate  $\eta$  is perpendicular to  $\xi$ . In the following, we will use the local distance  $\eta^*(\xi)$  between the leaflets to define the nondimensional coordinate  $\tilde{\eta} = \eta/\eta^*(\xi)$ , such that the inner sides of the leaflets are at  $\tilde{\eta} = \pm 1/2$ .

The temporal evolution of streamwise velocity profiles taken at  $\xi = 0.54$  mm is shown in the left panel of Fig. 5 at different times  $t$ . At later times ( $t > 20$  ms), the velocity profiles attain a self-similar shape. On the right panel of Fig. 5, normalized streamwise velocity profiles are illustrated at four streamwise locations ( $\xi_1 = 0.54$ ,  $\xi_2 = 1.08$ ,  $\xi_3 = 1.62$ ,  $\xi_4 = 2.16$  mm). With increasing distance from the separation point, these profiles become flatter and more self-similar. The profiles were taken at  $t = 29$  ms when vortex shedding had already started farther downstream. In general, the ILEV zone rapidly grows and stretches as the flow accelerates. The ILEV flow becomes oscillatory at approximately two-plate-thickness lengths downstream of the separation point. This waviness is more pronounced farther downstream and finally results in the shedding of larger vortices into the bulk flow, which travel nearly half as fast as the mean flow velocity. The streamwise and temporal evolution of vorticity waves obtained from 2D-DNS is illustrated in

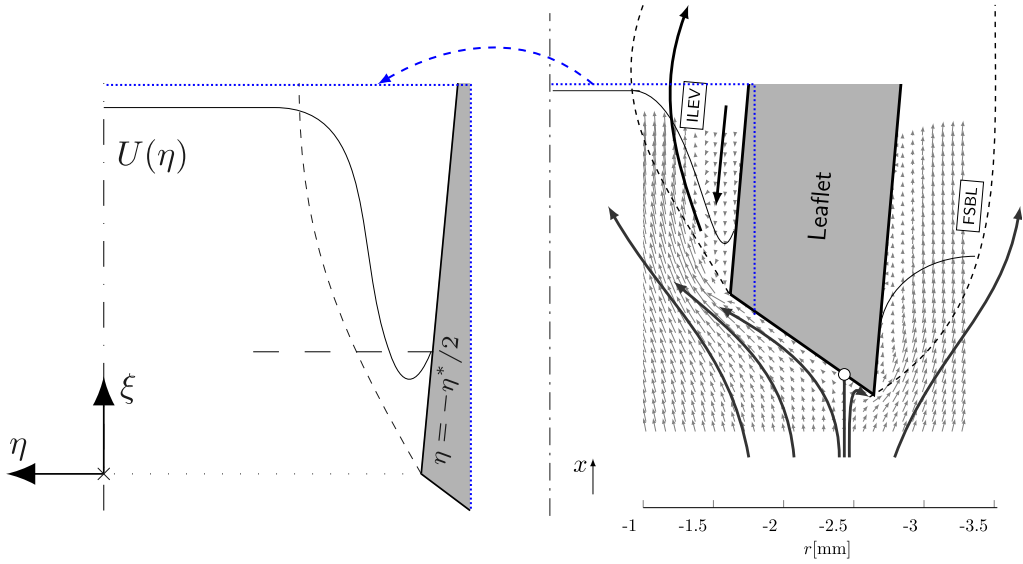


FIG. 4. Right: Fully resolved flow impingement resulting in an ILEV on the inner side of the leaflet near the leading edge. The stagnation point ( $\circ$ ) is closer to the outer side than the inner side of the leaflets, where the ILEV is located. Falkner-Skan boundary layers (FSBLs) remain attached on the outer side of the leaflets. The curved dashed line on the inner side shows the extent of the ILEV. The oscillatory tail of the ILEV is not shown here. The vertical dash-dotted line shows the centerline. Left: Local coordinate system used for the stability analysis within the laminar part of the ILEV.  $\xi$  is the streamwise axis whose origin is on the centerline at the  $x$  position of the separation point.  $\eta$  is the cross-stream axis, which extends between the two leaflets.  $U(\eta)$  shows a typical local streamwise velocity profile, which comprises a zone of reverse flow ( $U < 0$ ) near the leaflet surface and a zone of forward flow ( $U > 0$ ) towards the centerline.

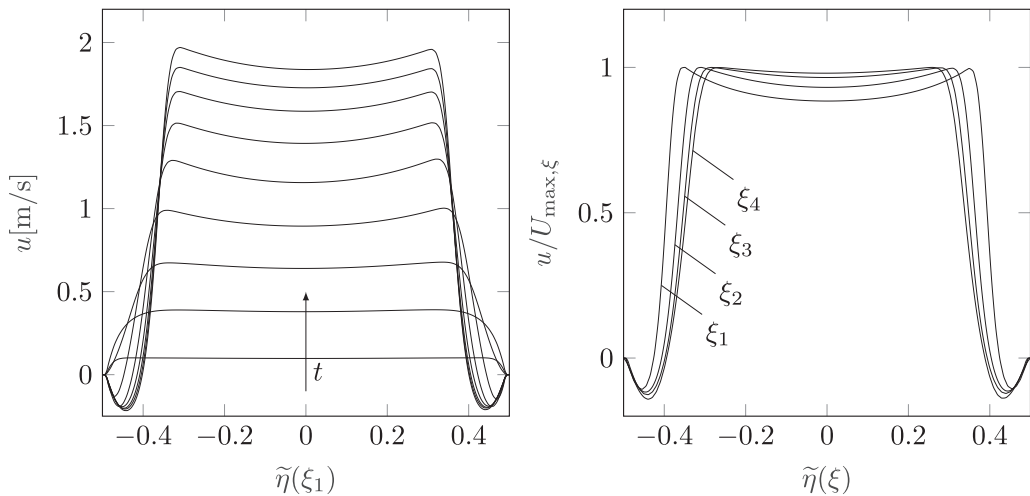


FIG. 5. Left: The temporal evolution of streamwise velocity profiles taken at  $\xi_1 = 0.54$  mm downstream of the separation point ( $\xi = 0$ ). The arrow with label  $t$  shows progress in time, starting from  $t = 1.4$  ms to  $t = 36$  ms, with marching step of 4.3 ms. Right: Streamwise velocity profiles taken at  $t = 29$  ms at four locations:  $\xi_1 = 0.54$  mm,  $\xi_2 = 1.08$  mm,  $\xi_3 = 1.62$  mm, and  $\xi_4 = 2.16$  mm.



Fig. 7. It shows vorticity data that were extracted from 2D-DNS along a line parallel to the  $\xi$  axis and originating at the separation point.

Flow separation at the leading edge of blunt flat plates has been addressed in several studies [10,12,13,29,42]. Cherry *et al.* [42] were among the first to measure the velocity and pressure fluctuations due to flow separation near the leading edge of blunt plates at Reynolds numbers as high as 32 000. They reported stretched bubbles forming downstream of the separation point, which maintained self-similar profiles until nearly 60% of the bubble length. Downstream of the bubble, they observed departures from self-similarity, which they attributed to reattachment effects. Nakamura *et al.* [10] have studied the flow around square-edged flat plates, with chord-to-thickness ratios ranging from 3 to 16, at Reynolds numbers (based on plate thickness) in the range of 1000 to 3000. Their smoke visualizations showed pronounced vortex shedding on the surface of the blunt plates, which they related to impinging shear-layer instability, that is, the instability of the separated shear layer due to interaction with a sharp trailing-edge corner. They also showed that for the chord-to-thickness ratio of 8, the structure of the separated shear layers near the blunt edge is first laminar and two dimensional. Ohya *et al.* [12] studied a similar problem at  $Re = 1000$ , and chord-to-thickness ratio ranging from 3 to 9 using two-dimensional numerical simulations. They confirmed that the impinging shear layer instability agrees well with experiments of Nakamura *et al.* [10]. It is worth mentioning that according to Stokes and Welsh [11], a nonsmooth leading edge featuring sharp corners is not the primary cause of flow separation, as that can also be triggered by smoothed leading-edge geometries. The mechanism of trailing-edge vortex shedding and the role it plays in completing a feedback loop by triggering the leading-edge instabilities was examined by Hourigan *et al.* [13]. These studies motivate similar investigations for the BMHV model, although there are several differences between the flow configurations, e.g., the nonzero angle of incidence, the nonsquare shape of the leading edge, the number of the plates, and their confinement within a bounded geometry.

### B. Role of spatial resolution on ILEV structures

Although ILEV structures are well documented by numerical simulations of canonical flows around blunt plates with aspect ratios similar to that in BMHVs (e.g., [13]), they have not been observed so far in the most numerical simulations of BMHVs (e.g., [6,9]), which may be due to insufficient spatial resolution around the leaflets. To the best of our knowledge, ILEV structures have been shown for BMHVs so far only by Zbavitel and Fialová [43], who demonstrated that these structures can only be captured with sufficiently resolved direct numerical simulations. They showed, in particular, that the unsteady Reynolds averaged Navier-Stokes (URANS) approach as opposed to DNS fails to resolve the flow instabilities between the valve leaflets. They further discussed the pronounced effect that these leading-edge instabilities have on the velocity magnitude in the wake, yet did not study the type and quantitative behavior of the instabilities (for instance, spatial and temporal frequencies) that they observed. In agreement with their finding that these structures are difficult to resolve numerically, we were able to confirm that ILEV instabilities are suppressed for too coarse spatial resolutions. Convergence (based on the local half wavelength of instability waves within the ILEV zone) was only found for at least 31 grid points per leaflet thickness, which corresponds to a uniform grid spacing of  $\delta_h = 35 \mu\text{m}$  (Fig. 6, left). The ratio of the converged grid spacing to the wavelength of the local ILEV instability ( $2\kappa_\xi$ ) was found to be  $\tilde{\delta}_{h,\kappa} = \delta_h/2\kappa_\xi \approx 0.035$ . Coarse simulations did not exhibit any waviness in the ILEV structures (cf. inset of Fig. 6, left). Likewise, we observed convergence for impinging streamwise velocity profiles taken at a cross section shortly upstream of the leading edge for similar levels of resolution (Fig. 6, right).

## IV. LINEAR STABILITY OF THE ILEV

### A. Viscous temporal instability

We proceed to investigate the linear temporal stability of the local velocity profiles in the ILEV. To make progress, we idealize the flow configuration and assume locally parallel flow. This

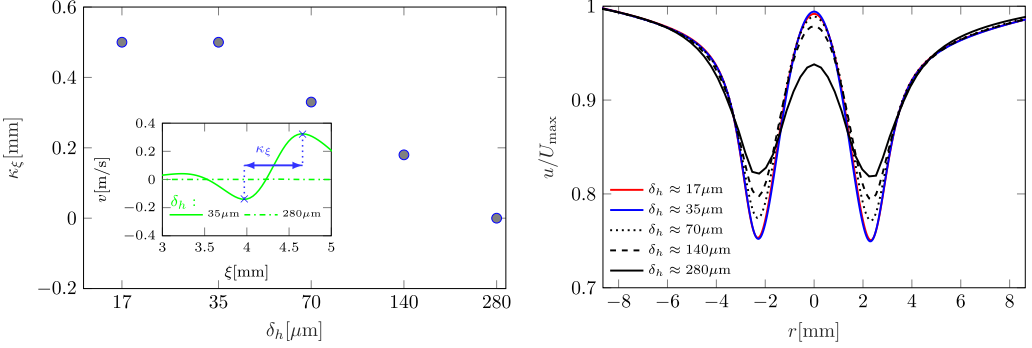


FIG. 6. Left: Effect of spatial resolution on the development of instability waves in the ILEV. This panel demonstrates the convergence of the local half wavelength  $\kappa_\xi$  in the function of the grid spacing  $\delta_h$ . The inset shows transversal velocity profiles for the converged simulation ( $\delta_h = 35 \mu\text{m}$ ) and for the coarsest grid ( $\delta_h = 280 \mu\text{m}$ ) slightly after the onset of oscillations at  $t = 35$  ms. Profiles are taken along a streamwise line extending from  $\xi = 3$  to  $5$  mm at a radial position of  $r = -1.08$  mm.  $\kappa_\xi$  is quantified in the same interval. No waviness is observed for the coarse simulation. Right: Convergence of the streamwise velocity profile slightly upstream of the separation point ( $\xi = -1.4$  mm) at  $t = 27$  ms.

assumption is justified here by the small angle of incidence of the leaflets ( $5^\circ$ ) and the high aspect ratio of the stretched recirculation zone between the leaflets. It will be further justified *a posteriori* by the good agreement between the results from local stability analysis with the nonlinear simulation data.

Substituting the parallel flow profile  $\tilde{U} = u(\xi_1, \eta, t_1)/U_{\max, \xi_1}$  at a given streamwise location  $\xi = \xi_1$  and at time  $t = t_1$  in the linearized Navier-Stokes equation leads to the classical Orr-Sommerfeld equation,

$$\{\mathcal{D}^4 - 2\tilde{\alpha}^2 \mathcal{D}^2 + \tilde{\alpha}^4 - i\tilde{\alpha} \text{Re}_\eta [(\tilde{U} - \tilde{c})(\mathcal{D}^2 - \tilde{\alpha}^2) - \tilde{U}''']\} \hat{v} = 0, \quad (4)$$

where  $\mathcal{D} = d/d\tilde{\eta}$ .  $\tilde{\alpha} = 2\pi/\tilde{\lambda}$  and  $\tilde{c} = \tilde{\omega}/\tilde{\alpha}$  are the complex wave number and phase speed in the disturbance ansatz  $[\hat{u}(\tilde{\eta}), \hat{v}(\tilde{\eta})]e^{i\tilde{\alpha}(\xi - \tilde{c}t)}$ . The reference velocity  $U_{\max, \xi}$  is the local maximum streamwise velocity at  $\xi$ . The local Reynolds number  $\text{Re}_\eta$  is then defined as

$$\text{Re}_\eta = \frac{U_{\max, \xi} \eta^*}{\nu}. \quad (5)$$

We seek temporal instability waves with  $\text{Im}(\tilde{c}) > 0$  and  $\tilde{\alpha} \in \mathbb{R}$ . To this end, we discretize Eq. (4) using sixth-order finite differences, which results in a complex generalized eigenvalue problem of the form

$$\mathbf{A}(\text{Re}_\eta, \tilde{U}, \tilde{\alpha}) \hat{\mathbf{v}} = -i\tilde{c} \mathbf{B}(\tilde{\alpha}) \hat{\mathbf{v}}. \quad (6)$$

Homogeneous boundary conditions

$$\hat{v}(\tilde{\eta}) = \partial_{\tilde{\eta}} \hat{v}(\tilde{\eta}) = 0, \quad \tilde{\eta} \in \left\{ 0, -\frac{1}{2} \right\}, \quad (7)$$

are discretized and integrated in  $\mathbf{A}$  and  $\mathbf{B}$ . To save computational time and owing to the prominent symmetry of the velocity profiles (cf. Fig. 5), only half of the profile is considered which is also reflected by the symmetry boundary condition at  $\tilde{\eta} = 0$ . We have computed the Orr-Sommerfeld (OS) spectrum for a few base flows spanning the full profile and verified that nearly double eigenvalues are recovered.

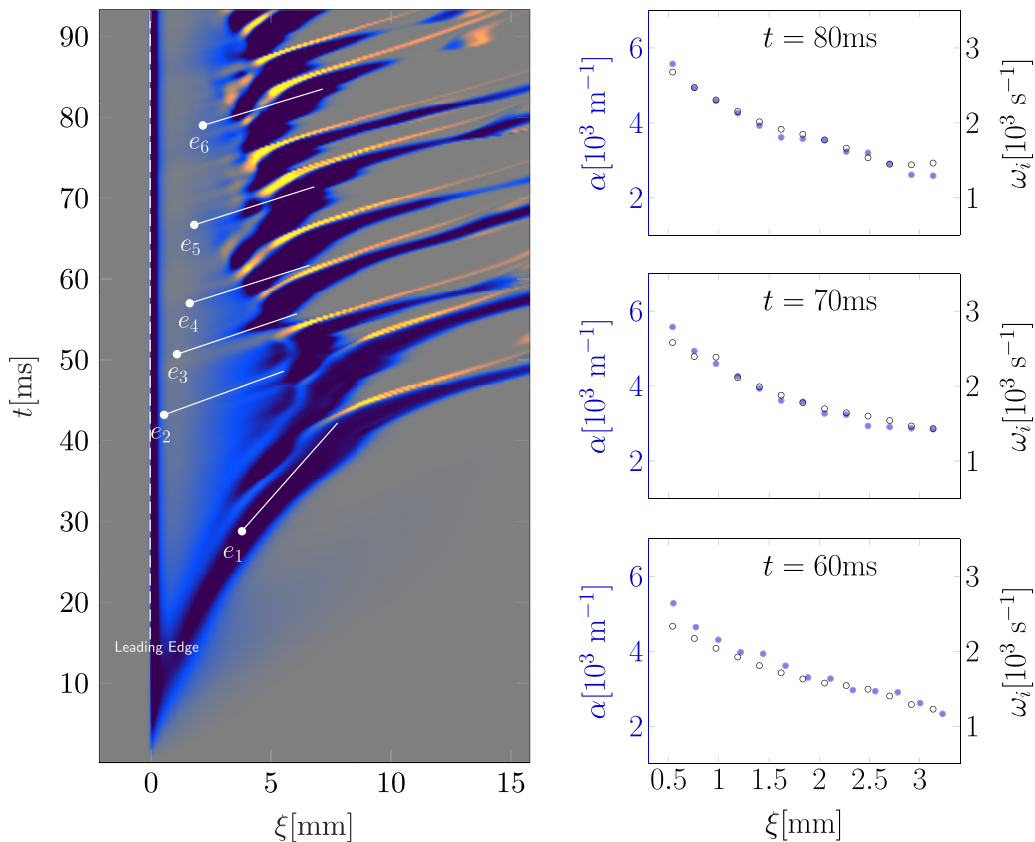


FIG. 7. Left: Vorticity waves evolving in time  $t$  and space  $\xi$  near the leading edge. Vorticity data are taken from 2D-DNS results along a line extending in the  $\xi$  direction from the separation point  $(\xi, \eta) = (0, 0 \text{ mm})$  to  $\xi = 16 \text{ mm}$ . The light yellow and dark blue colors on the background illustrate positive-maximum and negative-minimum vorticity, respectively. Solid white points indicate six base flows,  $e_{1,2,3,4,5,6}$ . The slopes of the solid white lines indicate the phase velocity of the corresponding least stable eigenmodes. Right: Dimensional local growth rates  $\omega_i = \alpha c_i$  ( $\circ$ , right axes) and wave numbers  $\alpha$  ( $\bullet$ , left axes) of the most unstable modes for base flows taken along the  $\xi$  axis at times  $t = 60, 70, 80 \text{ ms}$ .

It is not straightforward to extract base flow profiles from 2D-DNS in regions where strong instabilities and vortex shedding are present. This is the case on the downwind side of the ILEV (e.g.,  $\xi > 3 \text{ mm}$  in Fig. 7) and we will investigate the origin of such oscillations later in this paper. Meanwhile, we apply local temporal theory for the flow states where temporal flow oscillations are sufficiently small (less than 5% oscillations due to flow development or weak flapping). We have confirmed that these small oscillations have no significant effect on the computed growth rates of the instabilities. Figure 7 illustrates results for six different base flows obtained at six different positions  $\xi$  and times  $t$  (white points  $e_{1,\dots,6}$  on the left panel).

The phase speeds ( $c_r$ ) of the most unstable temporal eigenmodes are indicated by the white lines extending from the corresponding white points. A comparison of these results to the 2D-DNS data in Fig. 7 shows that parallel linear theory can offer a remarkably good prediction of the flow oscillations initiating after the separation point, as the white lines are well aligned with the adjacent vorticity traces observed in 2D-DNS. Numerical data for these modes are summarized in Table II.

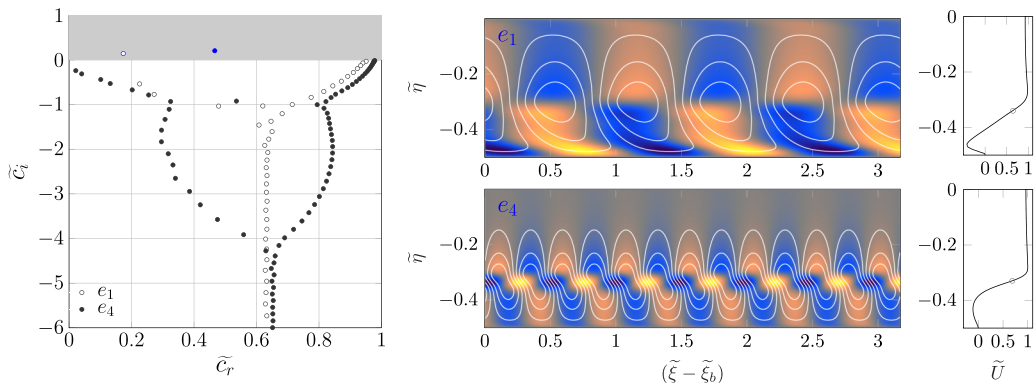


FIG. 8. Eigenvalue spectra (left) and the disturbance velocity field corresponding to the most unstable modes for base flows  $e_1$  (middle, top) and  $e_4$  (middle, bottom).  $\tilde{\xi}_b$  is the streamwise location of the base flow. The light yellow and dark blue colors on the background illustrate positive-maximum and negative-minimum streamwise velocity, respectively. The white lines show streamlines. Normalized base flow profiles are shown for  $e_1$  (right, top) and  $e_4$  (right, bottom). The location of inflection points ( $U'' = 0$ ) is marked with circles on the right panel.

In general, we find that nearly all base flows past the separation point are linearly unstable. This is illustrated in the right panel of Fig. 7, which shows growth rates  $\omega_i = \alpha c_i$  and wave numbers  $\alpha$  for various profiles along the  $\xi$  axis at three different points in time ( $t = 60, 70,$  and  $80$  ms). These results show that wave number and growth rate of the least stable mode decrease while moving downstream.

Note that the base flow  $e_1$  has been taken at a much earlier stage than the other base flows, where unsteady and oscillatory effects of the developing flow were quite strong. Nevertheless, the local stability analysis still produced results in good agreement with 2D-DNS data. The different stability characteristics of  $e_1$  are further illustrated in Fig. 8, where eigenvalue spectra and the streamwise disturbance velocity field corresponding to the most unstable eigenmodes of base flows  $e_1$  and  $e_4$  are shown on the left and middle panel, respectively (eigenfunctions and spectra for  $e_{2,3,4,5,6}$  are qualitatively the same as for  $e_4$ ). On the right panel of this figure, the base flow profiles for  $e_1$  and  $e_4$  are given. The middle and right panels of Fig. 8 show that the inflection point in the base flow profile  $U$  coincides in location with the maximum value of the streamwise velocity disturbance for  $e_4$  (as opposed to  $e_1$ ). This suggests that the unstable eigenmode for the  $e_4$  base flow has inviscid character (free shear-layer eigenmode), whereas the unstable eigenmode for the  $e_1$  base flow is probably of viscous character (Tollmien-Schlichting-type eigenmode). Such differences in the instability character have been attributed by Rist and Maucher [44] to the influence of the wall on the instabilities in the shear layer.

TABLE II. Characteristics of the base flows  $e_{1,2,3,4,5,6}$  and their associated most unstable modes (cf. Fig. 7).

Base flow	$t$ (ms)	$\xi$ (mm)	$\text{Re}_\eta$	$\alpha$ ( $\text{m}^{-1}$ )	$\tilde{\alpha}$	$\omega_{i,\text{max}}$ ( $\text{s}^{-1}$ )	$\tilde{\omega}_{i,\text{max}}$	$c_r$ (m/s)	$\tilde{c}_r$
$e_1$	29	3.78	2536	1250	5	310	0.72	0.30	0.17
$e_2$	43	0.54	2564	4294	18	2120	3.55	0.92	0.45
$e_3$	51	1.08	2779	4142	14.5	1847	3.02	1.00	0.46
$e_4$	57	1.61	2990	3611	13	1678	2.69	1.05	0.47
$e_5$	67	1.80	3103	3243	12	1575	2.54	1.07	0.47
$e_6$	76	2.16	3322	3571	12.5	1635	2.49	1.12	0.46

### B. *A posteriori* analysis for sufficient timescale separation

The applicability of the Orr-Sommerfeld equation is not guaranteed *per se* because it assumes that the base flow  $U$  is steady, whereas the studied base flow is accelerated. Therefore, here we demonstrate *a posteriori* that there exists sufficient timescale separation between the base flow and the growth of the unstable modes such that the base flow can be considered quasisteady for the stability analysis. The remarkable alignment of the theoretical results with 2D-DNS data can be taken as a supporting evidence that sufficient timescale separation of the perturbation modes occurs in this case. In addition to this qualitative evidence, we attempt to define a quantitative necessary criterion for ensuring timescale separation. Our analysis starts with the linear decomposition of the velocity field  $u$  to a base flow  $U$  and a perturbation  $u'$ ,

$$u = U + u', \quad (8)$$

with  $\|u'\| = \epsilon \|U\|$  and  $0 < \epsilon \ll 1$ ;  $\|\cdot\|$  is defined here as

$$\|f(\tilde{\eta})\| = \sqrt{\int_{-1/2}^{1/2} f(\tilde{\eta})f^*(\tilde{\eta})d\tilde{\eta}}, \quad (9)$$

where  $f^*$  denotes the complex conjugate of  $f$ . Introducing the normal-mode ansatz for a perturbation at  $\xi = \xi_b$  leads to

$$u(\xi_b, \eta, t) = U(\xi_b, \eta, t) + \hat{u}(\xi_b, \eta)e^{-i\omega t}. \quad (10)$$

Taking the time derivative of this equation gives

$$\partial_t u = \partial_t U - i\omega \hat{u}e^{-i\omega t}. \quad (11)$$

In order to have sufficient timescale separation, the first term on the right-hand side must be much smaller than the second term,

$$\|\partial_t U\| \ll \|-i\omega \hat{u}e^{-i\omega t}\|. \quad (12)$$

Dividing both parts of this inequality by  $\|U\|$  results in

$$\frac{\|\partial_t U\|}{\|U\|} \ll \frac{\|-i\omega \hat{u}e^{-i\omega t}\|}{\|U\|} \leq |\omega_i| \frac{\|\hat{u}e^{-i\omega t}\|}{\|U\|} = |\omega_i| \frac{\|u'\|}{\|U\|} = |\omega_i|\epsilon. \quad (13)$$

Therefore, for a disturbance to grow much faster than the base flow, it is necessary to have

$$\mathcal{G} = \frac{\|\partial_t U\|}{|\omega_i|\|U\|} \ll \epsilon \ll 1. \quad (14)$$

We compute  $\mathcal{G}$  for the base flows  $e_{1,\dots,6}$ . The results are plotted in Fig. 9. If we choose, for example,  $\epsilon = 0.1$ , we find that  $\mathcal{G} \ll \epsilon \ll 1$  is satisfied for all base flows except for  $e_1$ , where  $\mathcal{G} \approx 0.2$ . As mentioned before, this result is likely due to the rapid development of the ILEV at  $e_1$ . Nevertheless, a good agreement with 2D-DNS data was also found for this base flow (cf. Fig. 7). Therefore, we conclude from this *a posteriori* analysis that there is sufficient timescale separation between the base flow acceleration and hydrodynamic instabilities, and this justifies the applicability of the Orr-Sommerfeld equation (4).

## V. ABSOLUTE INSTABILITY OF THE ILEV

### A. A brief overview

Hourigan *et al.* [13] conjectured that the weak flapping of the separated shear layer from the leading edge of blunt plates [42] might be caused by local absolute instabilities. Even though Soria and Wu [45] showed that the instabilities in the ILEV are predominately of a convective nature, even a small pocket of absolute instability can act as a wave maker, which then contaminates the

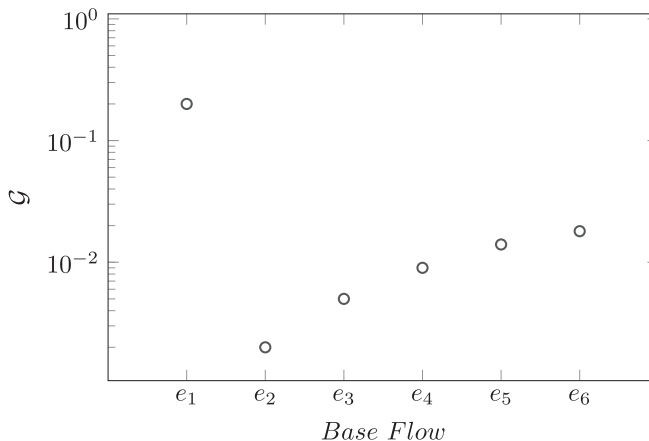


FIG. 9. The timescale separation parameter  $\mathcal{G}$  for six base flows,  $e_{1,2,3,4,5,6}$ .

flow with disturbances in downstream and upstream directions. We therefore study the absolute or convective nature of the flow instabilities in the ILEV developing in BMHVs.

### B. Mean flow calculation and the cusp map procedure

We aim at obtaining unperturbed base flow profiles of the extended ILEV region. Such base flow profiles must be extracted with great care from DNS or experimental data of a flow containing absolute instabilities because the flow fields are typically contaminated with strong fluctuations. Here, the stability analysis is performed on a mean flow field instead of an actual steady-state base flow because we were unable to achieve artificial stabilization of the ILEV in the BMHV model by selective frequency damping [46]. Several other studies have used mean flow fields as the base flow with excellent results (e.g., [47,48]), and some authors even preferred a mean flow over a steady-state base flow arguing that it factors in some nonlinear effects [49,50]. We obtain the mean flow by averaging the flow fields  $\mathbf{u}$  over time after normalizing them with respect to the maximum velocity  $U_{\max,\xi=0}(t)$  at the streamwise location  $\xi = 0$ ,

$$\bar{\mathbf{u}}(\xi, \eta) = \frac{1}{T} \int_{t_0}^{t_0+T} \frac{\mathbf{u}(\xi, \eta, t)}{U_{\max,\xi=0}(t)} dt. \quad (15)$$

Accordingly, we modify the Reynolds number  $Re_\eta$  [Eq. (5)] by using  $U_{\max,\xi=0}(t)$  as the reference velocity. Statistical invariance of the normalized averaged velocity fields is confirmed by comparing velocity fields which were averaged over different time intervals. The time-averaged flow field and velocity profiles taken at two locations within the ILEV are shown in Fig. 10. Slight asymmetries in the velocity profiles can be attributed to the cavities ( $\partial\Omega_{s,c}$ ), which are not symmetric. There exists a small secondary recirculation at  $\xi \approx 3.5$  mm.

For the absolute instability analysis, Eq. (4) is used as dispersion relation for the instability waves [ $\mathcal{D}(\tilde{\alpha}, \tilde{\omega}) = 0$ ]. The method of cusp maps [16] is utilized to identify the absolutely unstable profiles within the larger pool of convective instabilities. The cusp map procedure requires mapping from the  $\alpha$  plane to the  $\omega$  plane. To this end, a set of purely imaginary and parallel rays are selected in the complex  $\alpha$  plane such that their mappings in the  $\omega$  plane are located beneath the mapping  $\mathcal{L}$  of the Fourier-inversion contour  $\mathcal{F}$ , which is the contour obtained for  $\tilde{\alpha}_i = 0$ . The mappings of the  $\alpha$  rays eventually lose their angle-preserving property, which marks the presence of a branch point. Branch points with positive  $\tilde{\omega}_i$  indicate an absolute instability, whereas negative  $\tilde{\omega}_i$  correspond to convective instabilities.

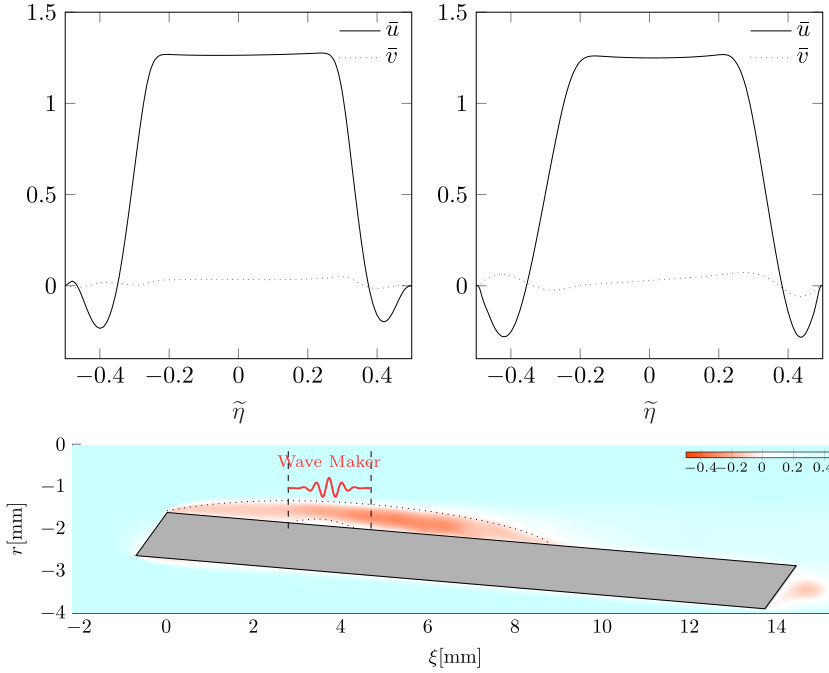


FIG. 10. Top: Time-averaged streamwise ( $\bar{u}$ ) and transversal ( $\bar{v}$ ) velocity profiles taken at  $\xi = 3.24$  mm (left) and  $\xi = 4.75$  mm (right). Bottom: Time-averaged normalized flow field used for the absolute instability analysis. Colors show the streamwise velocity (red: negative velocities). Dotted lines are the contours of zero streamwise velocity. Averaging is performed from  $t = 57$  to 100 ms.

Branch points were obtained for base flow profiles at multiple locations along the ILEV. The flow profiles taken in the range from  $\xi = 2.8$  to  $\xi = 4.7$  mm were found to be absolutely unstable. Although this range includes the secondary recirculation zone, we verified that the secondary circulation is not a necessary condition for the absolute instability. Exemplary cusp maps for two

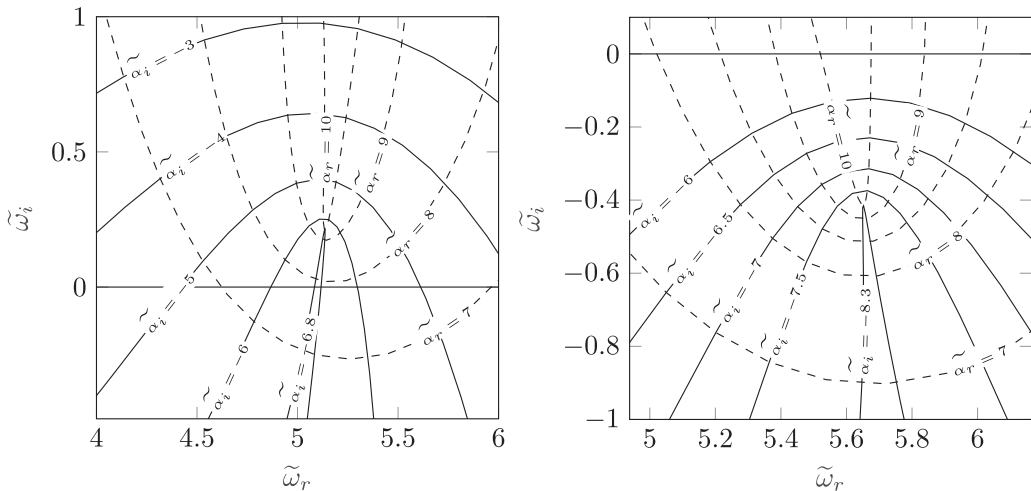


FIG. 11. Cusp maps for an absolutely unstable (left,  $\tilde{\alpha}_0 = 10.0 - 6.8i$ ,  $\tilde{\omega}_{i,0} = 0.22$ ) and a convectively unstable (right,  $\tilde{\alpha}_0 = 10 - 8.3i$ ,  $\tilde{\omega}_{i,0} = -0.4$ ) flow profile. The base flows for the left and right panels are taken  $\xi = 3.2$  mm and 2.7 mm, respectively.

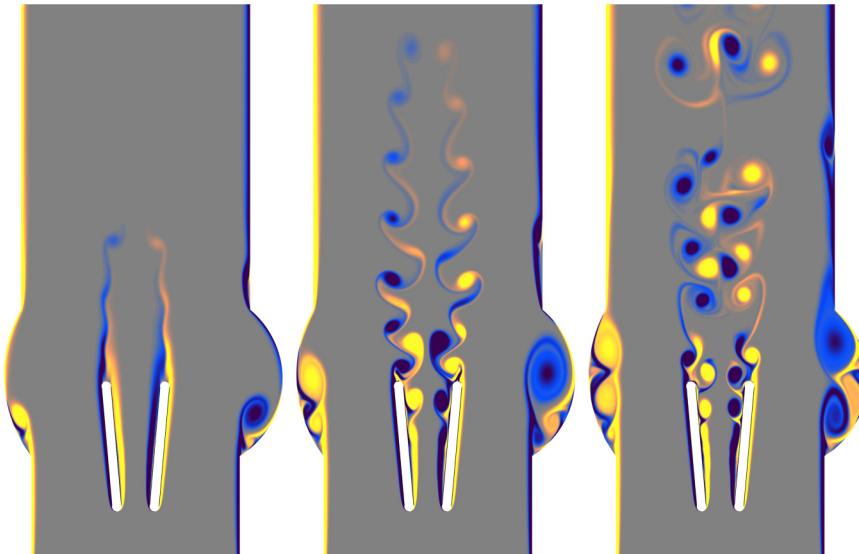


FIG. 12. Snapshots of vorticity (left to right:  $t = 35, 57, 79$  ms) when the leaflets' leading and trailing edges are rounded to circular profiles. Dark blue and light yellow show the vorticity extrema. The occurrence of the ILEV instability on the inner side of the leaflets is delayed and the location of oscillations is shifted farther downstream, but the instability is not eliminated.

base flows featuring convective and absolute instability are shown in Fig. 11. These results indicate the existence of a relatively large wave-maker region between the valve leaflets, which is collocated with the vortex shedding area observed in 2D-DNS.

### C. Absolute versus convective instabilities

#### 1. Making a simple case to eliminate the wave-maker region

As discussed earlier, Ref. [11] showed that vortex shedding at the leading edge of blunt plates can also occur for rounded geometries. We also show here by means of 2D-DNS that a circular shape for the leading edge only moves the ILEV instabilities farther downstream, but it does not eliminate the instability (Fig. 12). Therefore, the sharp edges of the BMHV leaflets may not be the primary cause for ILEV instabilities. We confirmed this in numerical experiments where the leading edges of the leaflets were smoothed. We found, for example, that a circular leading-edge geometry fails to eliminate the ILEV instabilities. Alternatively, we modified the leaflet geometry as shown in Fig. 13, with the aim of decreasing the cross-stream component of the impinging flow. To this end, the wedge geometry of the leading edge extends to  $\xi = l_l/2$ , which corresponds to the approximate time-averaged length of the ILEV. This modified geometry moves the sharp corner  $C$  farther downstream beyond the wave-maker region identified in the previous section. Similar to the  $\xi$  axis defined in Fig. 4, we introduce a coordinate  $\zeta$  with an origin located at  $C'$ .

We show in the following that this modification successfully eliminates the vortex shedding between the leaflets. It will also be shown that this stabilization of the flow between the leaflets leads to a sustained laminar flow in the wake of the leaflets.

#### 2. Simulation of the flow in the modified geometry

We perform a 2D-DNS of the flow in the modified leaflet geometry using the same pulse form shown in Fig. 2(b) and using the same spatial resolution as for the original geometry.



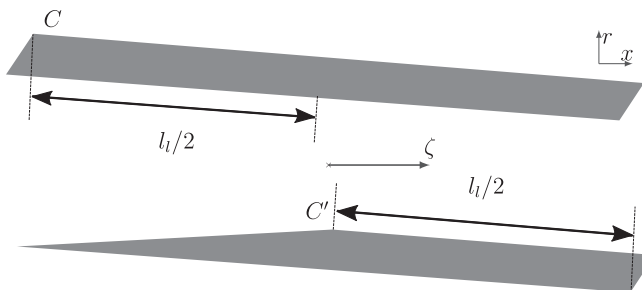


FIG. 13. Original (top) and modified (bottom) leaflet geometries for passive control of ILEV instabilities. The leaflet body is more streamlined, such that the separation point  $C$  is moved nearly one-thickness-length downstream of the wave-maker zone, to point  $C'$ .

The flow in the modified geometry showed no sign of flow separation between the leaflets. Reverse flow zones ( $U < 0$ ) adjacent to the leaflets were no longer presented (Fig. 14) and no vortices can be observed between the leaflets.

Figure 15 shows that the absence of the vorticity waves originating from the ILEV resulted in maintained laminar vortex structures in the wake of the leaflets. It is seen, however, that the vorticity profiles have evolved from Burgers-like structures (Fig. 3) to von Kármán-type vortex streets [Fig. 15(b)] due to continuous viscous straining. It is verified that the vortex streets remain structured and exhibit spatial decay.

Finally, we examine the linear stability of the flow between the modified leaflets. We resort to the same assumptions made in Sec. IV to study the temporal instability of the emerging flow profiles downstream of point  $C'$  in Fig. 13. No growing temporal modes were found up until approximately 0.6 mm downstream of  $C'$  [Fig. 15(c)]. Instability modes were identified farther downstream, which were all found to be of the convective type. The lack of absolute instabilities may explain why the modified geometry did not produce any vorticity between the leaflets.

## VI. CONCLUSIONS

The linear instability of the impinging leading edge vortices (ILEVs) developing at the leading edge of the blunt leaflets of a bileaflet mechanical heart valve has been investigated. A two-

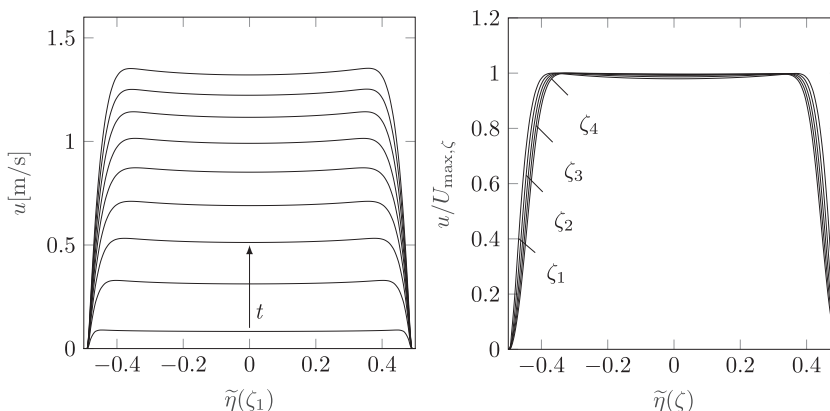


FIG. 14. Left: The evolution of streamwise velocity profiles taken at  $\zeta_1 = 0.54$  mm. The arrow with label  $t$  shows progress in time, starting from  $t = 1.4$  to  $t = 36$  ms, with marching step of 4.3 ms. Right: Normalized streamwise velocity profiles are taken at  $t = 29$  ms, for four locations:  $\zeta_1 = 0.54$ ,  $\zeta_2 = 1.08$ ,  $\zeta_3 = 1.62$ , and  $\zeta_4 = 2.16$  mm.

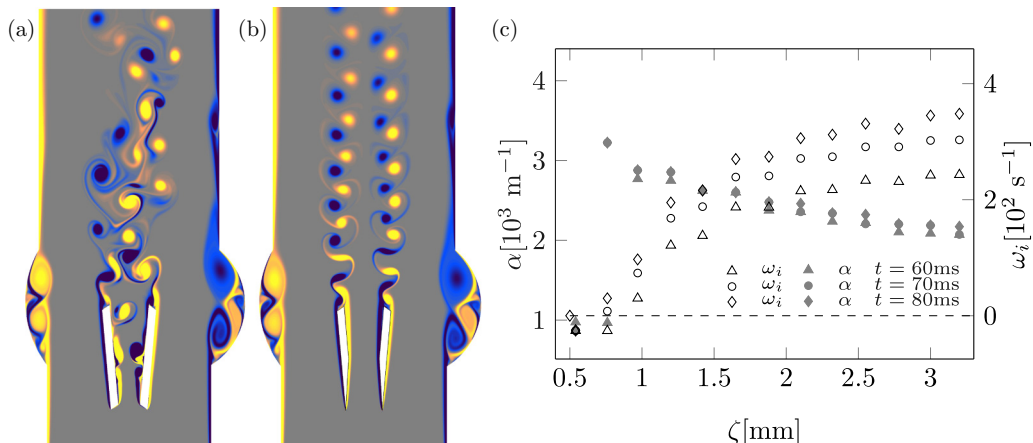


FIG. 15. Vorticity fields for the (a) current design and (b) proposed leaflet geometry of the BMHV. The modification has resulted in complete elimination of the ILEV, its instabilities, and the breakdown behind the valve model. (c) Growth rates  $\omega_i$  (hollow symbols) and their associated wave numbers  $\alpha$  (solid symbols) are plotted for the least-stable modes at various locations downstream of the roughness point  $C'$ , at times  $t = 60$  ms ( $\Delta$ ),  $t = 70$  ms ( $\circ$ ), and  $t = 80$  ms ( $\diamond$ ).

dimensional submodel of the valve is defined to be able to study the systolic ILEV instabilities close to the center of the leaflets. By means of high-order direct numerical simulations performed on very high-resolution grids, an unstable ILEV has been identified on the inner side of the valve leaflets. The stretched ILEV caused active vortex shedding between the leaflets. These vortical structures grew in size and interacted with organized Burgers-like vortices in the wake of the leaflets. This interaction resulted in the full breakdown of otherwise stable wake structures into disorganized small-scale vortices. The temporal instability of the ILEV was investigated using viscous parallel theory, where Orr-Sommerfeld eigenmodes were calculated for locations within the laminar part of the ILEV. Base flow profiles were extracted from 2D-DNS. Orr-Sommerfeld eigenmodes of positive growth have been obtained for all profiles along the laminar part of the ILEV. Despite several idealizations, the results of local linear stability theory agreed well with 2D-DNS. The method of cusp maps was then applied to time-averaged flow profiles along the ILEV, where pockets of absolute instability were identified. A modification in the leading-edge geometry was shown to eliminate ILEV instabilities, which resulted in maintained laminar flow behind the valve. The present study clearly illustrates the potential of applying the tools of hydrodynamic stability theory and laminar flow control to heart valve design.

#### ACKNOWLEDGMENTS

The authors acknowledge the Platform for Advanced Scientific Computing (PASC) for funding this work through the AV-FLOW and HPC-PREDICT projects. We are also grateful to the Swiss National Supercomputing Centre (CSCS) for providing technical support and GPU-node resources on the Cray XC40/50 supercomputer Piz Daint.

- [1] A. P. Yoganathan, Z. He, and S. Casey Jones, Fluid mechanics of heart valves, *Annu. Rev. Biomed. Eng.* **6**, 331 (2004).
- [2] F. Sotiropoulos, T. B. Le, and A. Gilmanov, Fluid mechanics of heart valves and their replacements, *Annu. Rev. Fluid Mech.* **48**, 259 (2016).

- [3] L. P. Dasi, L. Ge, H. A. Simon, F. Sotiropoulos, and A. P. Yoganathan, Vorticity dynamics of a bileaflet mechanical heart valve in an axisymmetric aorta, *Phys. Fluids* **19**, 067105 (2007).
- [4] L. Ge, H. Leo, F. Sotiropoulos, and A. P. Yoganathan, Flow in a mechanical bileaflet heart valve at laminar and near-peak systole flow rates: CFD simulations and experiments, *J. Biomech. Eng.* **127**, 782 (2005).
- [5] A. Bellofiore, E. M. Donohue, and N. J. Quinlan, Scale-up of an unsteady flow field for enhanced spatial and temporal resolution of PIV measurements: Application to leaflet wake flow in a mechanical heart valve, *Expt. Fluids* **51**, 161 (2011).
- [6] D. Bluestein, E. Rambod, and M. Gharib, Vortex shedding as a mechanism for free emboli formation in mechanical heart valves, *J. Biomech. Eng.* **122**, 125 (2000).
- [7] I. Borazjani, L. Ge, and F. Sotiropoulos, Curvilinear immersed boundary method for simulating fluid structure interaction with complex 3D rigid bodies, *J. Comput. Phys.* **227**, 7587 (2008).
- [8] I. Borazjani, Fluid-structure interaction, immersed boundary-finite element method simulations of bio-prosthetic heart valves, *Comput. Methods Appl. Mech. Eng.* **257**, 103 (2013).
- [9] M. Hedayat and I. Borazjani, Comparison of platelet activation through hinge vs bulk flow in bileaflet mechanical heart valves, *J. Biomech.* **83**, 280 (2019).
- [10] Y. Nakamura, Y. Ohya, and H. Tsuruta, Experiments on vortex shedding from flat plates with square leading and trailing edges, *J. Fluid Mech.* **222**, 437 (1991).
- [11] A. N. Stokes and M. C. Welsh, Flow-resonant sound interaction in a duct containing a plate, II: Square leading edge, *J. Sound Vib.* **104**, 55 (1986).
- [12] Y. Ohya, Y. Nakamura, S. Ozono, H. Tsuruta, and R. Nakayama, A numerical study of vortex shedding from flat plates with square leading and trailing edges, *J. Fluid Mech.* **236**, 445 (1992).
- [13] K. Hourigan, M. C. Thompson, and B. T. Tan, Self-sustained oscillations in flows around long blunt plates, *J. Fluids Struct.* **15**, 387 (2001).
- [14] E. Naudascher and Y. Wang, Flow-induced vibrations of prismatic bodies and grids of prisms, *J. Fluids Struct.* **7**, 341 (1993).
- [15] J. Soria, M. Sheridan, and J. Wu, Spatial evolution of the separated shear layer from a square leading-edge flat plate, *J. Wind Eng. Ind. Aerod.* **49**, 237 (1993).
- [16] K. Kupfer, A. Bers, and A. K. Ram, The cusp map in the complex-frequency plane for absolute instabilities, *Phys. Fluids* **30**, 3075 (1987).
- [17] <https://www.structuralheartsolutions.com/us/index.php?id=161&L=0>.
- [18] R. Henniger, D. Obrist, and L. Kleiser, High-order accurate solution of the incompressible Navier-Stokes equations on massively parallel computers, *J. Comput. Phys.* **229**, 3543 (2010).
- [19] R. Henniger, L. Kleiser, and E. Meiburg, Direct numerical simulations of particle transport in a model estuary, *J. Turbul.* **11**, N39 (2010).
- [20] M. O. John, D. Obrist, and L. Kleiser, Secondary instability and subcritical transition of the leading-edge boundary layer, *J. Fluid Mech.* **792**, 682 (2016).
- [21] M. O. John, D. Obrist, and L. Kleiser, Stabilisation of subcritical bypass transition in the leading-edge boundary layer by suction, *J. Turbul.* **15**, 795 (2014).
- [22] D. Obrist, R. Henniger, and L. Kleiser, Subcritical spatial transition of swept Hiemenz flow, *Int. J. Heat. Fluid Fl.* **35**, 61 (2012).
- [23] H. Zolfaghari, B. Becsek, M. G. Nestola, W. B. Sawyer, R. Krause, and D. Obrist, High-order accurate simulation of incompressible turbulent flows on many parallel GPUs of a hybrid-node supercomputer, *Comput. Phys. Commun.* **244**, 132 (2019).
- [24] H. Zolfaghari, D. Izbassarov, and M. Muradoglu, Simulations of viscoelastic two-phase flows in complex geometries, *Comput. Fluids* **156**, 548 (2017).
- [25] R. Mittal and G. Iaccarino, Immersed boundary methods, *Annu. Rev. Fluid Mech.* **37**, 239 (2005).
- [26] R. Mittal, H. Dong, M. Bozkurtas, F. M. Najjar, A. Vargas, and A. von Loebbecke, A versatile sharp interface immersed boundary method for incompressible flows with complex boundaries, *J. Comput. Phys.* **227**, 4825 (2008).
- [27] B. Vennemann, T. Rösgen, P. P. Heinisch, and D. Obrist, Leaflet kinematics of mechanical and bioprosthetic aortic valve prostheses, *ASAIO J.* **64**, 651 (2018).

- [28] B. M. Yun, L. P. Dasi, C. K. Aidun, and A. P. Yoganathan, Highly resolved pulsatile flows through prosthetic heart valves using the entropic lattice-Boltzmann method, *J. Fluid Mech.* **754**, 122 (2014).
- [29] S. Deniz and T. Staubli, Oscillating rectangular and octagonal profiles: Interaction of leading-and trailing-edge vortex formation, *J. Fluids Struct.* **11**, 3 (1997).
- [30] H. Hatoum, P. Maureira, and L. P. Dasi, A turbulence in vitro assessment of On-X and St. Jude Medical prostheses, *J. Thorac. Cardiovasc. Surg.* (2019), doi:[10.1016/j.jtcvs.2019.02.046](https://doi.org/10.1016/j.jtcvs.2019.02.046).
- [31] M. D. de Tullio, 68th Annual Meeting of the APS Division of Fluid Dynamics, November 22–24, 2015, <https://gfm.aps.org/meetings/dfd-2015/55f2d15c69702d060db60200>.
- [32] R. Haj-Ali, G. Marom, S. B. Zekry, M. Rosenfeld, and E. Raanani, A general three-dimensional parametric geometry of the native aortic valve and root for biomechanical modeling, *J. Biomech.* **45**, 2392 (2012).
- [33] J. Nordström, N. Nordin, and D. Henningson, The fringe region technique and the fourier method used in the direct numerical simulation of spatially evolving viscous flows, *SIAM J. Sci. Comput.* **20**, 1365 (1999).
- [34] G. K. Batchelor, *An Introduction to Fluid Dynamics* (Cambridge University Press, Cambridge, 2000).
- [35] P. J. Schmid and M. Rossi, Three-dimensional stability of a burgers vortex, *J. Fluid Mech.* **500**, 103 (2004).
- [36] T. Gallay and Y. Maekawa, Three-dimensional stability of burgers vortices, *Commun. Math. Phys.* **302**, 477 (2011).
- [37] E. Lamballais, J. Silvestrini, and S. Laizet, Direct numerical simulation of a separation bubble on a rounded finite-width leading edge, *Int. J. Heat. Fluid Fl.* **29**, 612 (2008).
- [38] L. E. Jones, R. D. Sandberg, and N. D. Sandham, Direct numerical simulations of forced and unforced separation bubbles on an airfoil at incidence, *J. Fluid Mech.* **602**, 175 (2008).
- [39] M. Alam and N. D. Sandham, Direct numerical simulation of short laminar separation bubbles with turbulent reattachment, *J. Fluid Mech.* **410**, 1 (2000).
- [40] N. D. Sandham, Transitional separation bubbles and unsteady aspects of aerofoil stall, *Aeronaut J.* **112**, 395 (2008).
- [41] V. Theofilis, S. Hein, and U. Dallmann, On the origins of unsteadiness and three-dimensionality in a laminar separation bubble, *Philos. Trans. A Math. Phys. Eng. Sci.* **358**, 3229 (2000).
- [42] N. J. Cherry, R. Hillier, and M. E. M. P. Latour, Unsteady measurements in a separated and reattaching flow, *J. Fluid Mech.* **144**, 13 (1984).
- [43] J. Zbavitel and S. Fialová, A numerical study of hemodynamic effects on the bileaflet mechanical heart valve, in *EPJ Web of Conferences*, Vol. 213 (EDP Sciences, Les Ulis, France, 2019), p. 02103.
- [44] U. Rist and U. Maucher, Investigations of time-growing instabilities in laminar separation bubbles, *Eur. J. Mech. B Fluids* **21**, 495 (2002).
- [45] J. Soria and J. Wu, The character of the instability of the separated shear layer from a square leading edge flat plate, in *Proceedings of 11th Australasian Fluid Mechanics Conference* (1992), pp. 14–18.
- [46] E. Åkervik, L. Brandt, D. S. Henningson, J. Høpfner, O. Marxen, and P. Schlatter, Steady solutions of the Navier-Stokes equations by selective frequency damping, *Phys. Fluids* **18**, 068102 (2006).
- [47] D. Barkley, Linear analysis of the cylinder wake mean flow, *Europhys. Lett.* **75**, 750 (2006).
- [48] B. Pier, On the frequency selection of finite-amplitude vortex shedding in the cylinder wake, *J. Fluid Mech.* **458**, 407 (2002).
- [49] S. Mittal, Global linear stability analysis of time-averaged flows, *Int. J. Numer. Methods Fluids* **58**, 111 (2008).
- [50] G. Mattingly and W. Criminale, The stability of an incompressible two-dimensional wake, *J. Fluid Mech.* **51**, 233 (1972).